remote sensing

MDPI

Article

Characteristics of the Wind Field and Low-Level Jets in the Middle and Lower Troposphere over Chengdu, Southwest China

Tao Du [1,2,*], Chen Wang [3], Xiaoyu Hu [4], Pengfei Tian [3], Yan Ren [5], Yunfan Song [1,2] and Jiajing Du [1,2]

1 Heavy Rain and Drought-Flood Disasters in Plateau and Basin Key Laboratory of Sichuan Province, Institute of Tibetan Plateau Meteorology, China Meteorological Administration, Chengdu 610072, China; songyf91@gmail.com (Y.S.); dujiajing@cma.gov.cn (J.D.)
2 Institute of Tibetan Plateau Meteorology, Chinese Academy of Meteorological Sciences, Beijing 100081, China
3 College of Atmospheric Sciences, Lanzhou University, Lanzhou 730000, China; wangch202115@163.com (C.W.)
4 Chongqing Research Institute of Big Data, Peking University, Chongqing 401329, China
5 Collaborative Innovation Center for Western Ecological Safety, Lanzhou University, Lanzhou 730000, China; ry@lzu.edu.cn
* Correspondence: dutao@cma.gov.cn

Highlights

What are the main findings?

- The RWP achieves an annual effective detection height of 7.4 km over the western Sichuan Basin, showing good consistency with radiosonde data.
- High-resolution vertical wind structure over the Chengdu basin reveals that horizontal wind speed accelerates markedly above 3 km (strongest in winter), and low-level winds shift from mountain-valley breezes to westerly winds aloft.
- LLJ occurrence peaks in July (followed by April), jet core heights range from 0.7 to 1.9 km, and for weaker LLJs, both frequency and intensity are higher at night than during the day.

What are the implications of the main findings?

- These findings deepen our understanding of boundary layer dynamics over complex basin terrain and provide a high-resolution observational benchmark for model improvements.
- The results offer scientific support for heavy rainfall warnings, air pollution management, and the safe operation of the low-altitude economy.

Abstract

Low-level jets (LLJs) play an important role in the transport of heat, water vapor, and atmospheric pollutants. Based on one year (1 September 2023 to 31 August 2024) of tropospheric wind profiler radar (RWP) observations at the Wenjiang Meteorological Observation Base in Chengdu, this study systematically investigates the wind field structure in the middle and lower troposphere over the Chengdu region and the vertical distribution and evolution characteristics of LLJs. The effective detection height of the RWP reaches at least 7.4 km throughout the year, demonstrating good consistency with concurrent radiosonde data. Horizontal wind speed accelerates markedly above 3 km, with the strongest vertical gradient observed in winter. In the lower layer, the prevailing wind direction is primarily controlled by mountain-valley breezes; with increasing altitude, the westerly belt gradually becomes the dominant wind system. Within the atmospheric boundary layer (below 1 km), the wind field exhibits a distinct diurnal cycle: easterly winds dominate in the afternoon, shifting to northerly winds at night. Surface wind speed peaks in the afternoon, whereas upper-level wind speed peaks at night. The occurrence frequency of LLJs is highest in July

Check for updates

Academic Editors: Jinlong Yuan and Jiafeng Zheng

Received: 22 April 2026
Revised: 21 May 2026
Accepted: 27 May 2026
Published: 29 May 2026

(26.3% for LLJ-1), followed by April (17.8%). The prevailing wind directions of LLJs are north-northeasterly and northeasterly, and jet core heights are mainly distributed between 0.7 and 1.9 km. For weaker LLJs (LLJ-1 and LLJ-2), both frequency and intensity are higher at night than during the day, peaking at 22:00. These findings deepen our understanding of boundary layer dynamics over complex basin terrain and provide a high-resolution observational benchmark for model improvements and weather warnings.

Keywords: wind field characteristics; low-level jets; radar wind profiler; temporal variation; mountain-valley wind circulation

1. Introduction

Observing atmospheric wind profiles is essential for a wide range of applications, including the prediction of extreme rainfall, the tracking of tropical cyclones and hurricanes, the analysis of persistent haze pollution, and the study of complex aerosol-cloud-precipitation interactions [1–6]. Among various meteorological phenomena, low-level jets (LLJs) stand out as particularly influential on a global scale [7–12]. The pronounced vertical wind shear associated with LLJs can generate intermittent turbulence near the surface and alter the vertical exchange of heat, moisture, and pollutants. Consequently, LLJs significantly affect pollutant dispersion, the urban heat island effect, wind power generation, aircraft operations, and heavy rainfall events [13–16]. Multiple mechanisms act together to produce LLJs, such as inertial oscillations, thermally induced topographic forcing, and large-scale synoptic processes [17–22].

The characteristics of wind fields in the middle and lower troposphere are governed by a range of factors, including atmospheric dynamics, thermal conditions, topography, underlying surface properties, and anthropogenic influences [23–25]. In recent years, numerous studies have employed diverse datasets to investigate tropospheric wind fields across different regions worldwide [26–30]. For instance, Yan (2021) [30] identified six regions in China with high-frequency LLJs using long-term radiosonde observations. Zheng (2024) [23] employed Doppler wind lidar to reveal that the dominant near-surface wind direction in the lower troposphere over Xining is primarily influenced by valley-mountain circulation. Radar wind profiler (RWP), which operates based on the scattering of electromagnetic waves by atmospheric turbulence, enables real-time, continuous monitoring of three-dimensional wind field information in the upper atmosphere [31–33]. Compared with conventional ground-based in situ observations (e.g., anemometers) and remote sensing techniques (e.g., Doppler wind lidar), RWP offers two distinct advantages. First, it can provide continuous vertical profiles of wind fields up to the upper troposphere (typically 8–10 km) and is less affected by precipitation or low clouds—whereas lidar is significantly attenuated by clouds and precipitation. Second, it achieves a high temporal resolution at the minute level, which is much finer than that of conventional radiosonde observations (typically twice daily). These advantages make RWP particularly suitable for the long-term statistical analysis of wind field characteristics and LLJs. Consequently, wind profiler measurements have been successfully applied in various contexts, including air quality studies and weather forecasting [34–40]. For example, Wei (2014) [39] conducted a comparative analysis of LLJ characteristics in Tianjin and Shanghai using RWP data, revealing that nighttime LLJs are significantly stronger and more frequent than daytime occurrences. Similarly, Miao (2018) [40] systematically investigated LLJ characteristics in Beijing and Guangzhou using RWP observations. Yang (2025) [41] performed statistical analyses of the vertical distribution of wind fields and wind shear characteristics based on

RWP data. Li (2026) [42] revealed the nationwide variability of LLJs prior to warm-season nocturnal rainfall in China by RWP.

Chengdu is located in the western part of the Sichuan Basin. It features complex topography, bordering the eastern margin of the Qinghai–Tibet Plateau to the west and the Longquan Mountains to the east, and has a distinctive climate. Moreover, Chengdu has a permanent resident population of over 21 million and a relatively high population density. The wind field structure in the middle and lower troposphere over this region, particularly the LLJ, plays a critical role in the occurrence of local hazardous events, including persistent heavy rainfall, haze pollution, and low-level wind shear. Existing studies on the Chengdu area have primarily focused on the characteristics of the low-level wind field and its relationships with heavy precipitation or pollution processes [43–48]. However, systematic research specifically targeting the features of LLJs in this region is still lacking. This study utilizes one full year of RWP data to systematically analyze the vertical structure, seasonal variations, and diurnal variations in the wind field and LLJs over Chengdu, and fills the gap in characterization of LLJs in this region.

This study utilizes one year of high spatiotemporal resolution RWP observation data from a representative site in the Chengdu region (the Wenjiang Meteorological Observation Base). It systematically investigates the vertical distribution and evolution characteristics of the wind field and LLJs in the middle and lower troposphere, aiming to provide support for local meteorological operations, related scientific research, and low-altitude meteorological applications. The structure of this paper is as follows: Section 2 introduces the study area, observation instruments, data, and methods. Section 3 provides a detailed analysis of the wind field in the middle and lower troposphere over the Chengdu region, as well as the vertical distribution and evolution characteristics of LLJs. Section 4 presents the discussion. Section 5 summarizes the main conclusions.

2. Materials and Methods

2.1. Observation Site, Instrument, and Measurement

This study uses one year of observational data (1 September 2023 to 31 August 2024) from the Wenjiang Meteorological Observation Base in Chengdu (103.861°E, 30.749°N, 548.9 m above sea level), including balloon soundings, RWP observations, and surface wind data (Figure 1). The site is located in the northwestern Chengdu Plain, with flat, open terrain and a rural underlying surface. The sounding and RWP stations are about 50 m apart. The RWP (TWP8-L, Beijing METSTAR Radar Co., Ltd., Beijing, China; parameters in Table 1) retrieves horizontal wind speed (HWS), horizontal wind direction (HWD), and vertical wind speed (VWS) at 42 height levels up to about 8 km, with vertical resolutions of 120 m below 2 km and 240 m above 2 km. The RWP provides 6 min, 30 min, and 1 h averaged data [34]. Because minute-scale data contain transient atmospheric fluctuations [39,49], this study uses hourly averaged observations that have passed the manufacturer's 100% confidence test. To investigate seasonal differences, the data are divided into four seasons: spring (MAM), summer (JJA), autumn (SON), and winter (DJF).

Table 1. Main Technical Parameters of the TWP8-L Wind Profiling Radar System.

Parameters	Technical Performance Indicators
Radar System	Fully Coherent Pulse Doppler System
Operating Frequency	1290 MHz
Maximum Detection Altitude	≥3 km
Minimum Detection Altitude	≤100 m
Measurement Performance	Wind Speed Measurement Range: 0–60 m/s; Wind Direction Measurement Range: 0–360°

https://doi.org/10.3390/rs18111744

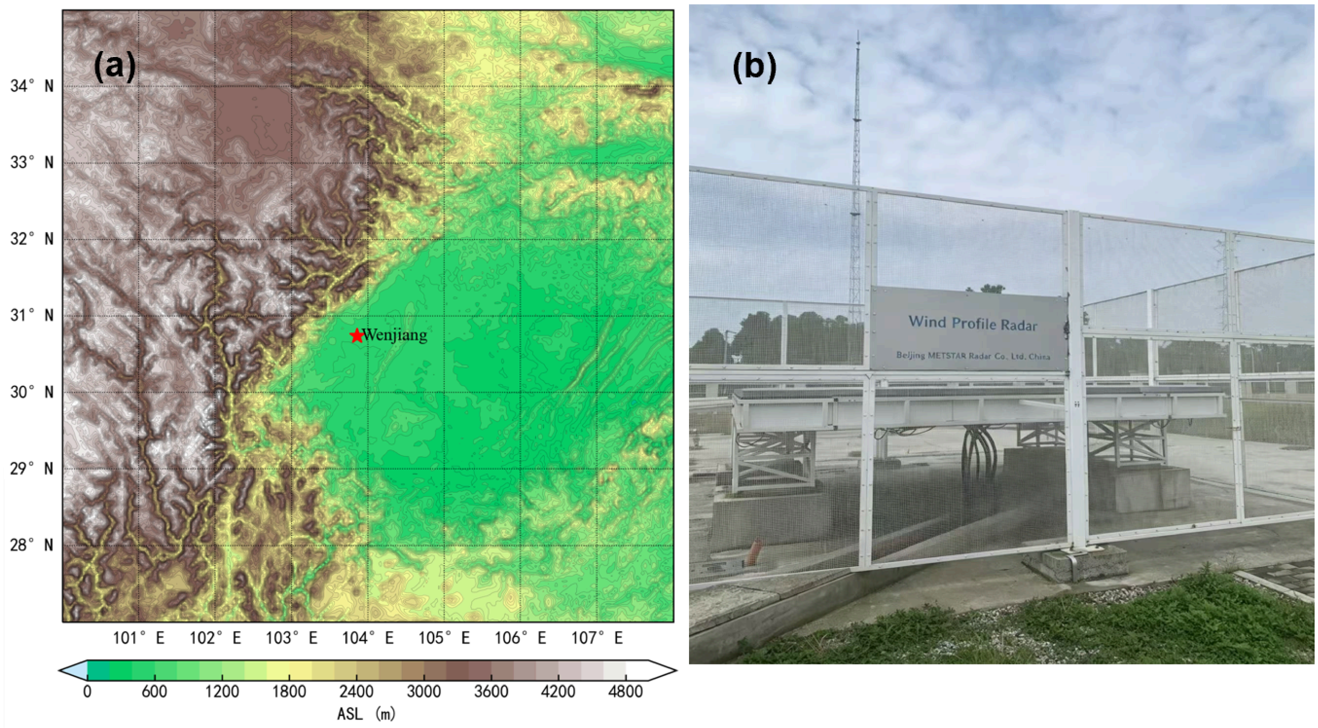

Figure 1. (**a**) Terrain of the Chengdu Wenjiang Meteorological Observation Base and (**b**) RWP.

2.2. Radar Wind Profiler Data Quality Control

The wind profiler data underwent strict quality assurance based on the methodology outlined by Wei (2014) [39]. Initially, each hourly wind profile was examined, and any profile with more than 40% of its data points identified as anomalies or missing was discarded. Subsequently, extreme outliers were removed when their variance within a given time window or altitude interval deviated from the mean by more than 2.5 standard deviations. Finally, data gaps were filled using linear interpolation. After quality control, a total of 8431 valid hourly wind profile datasets were obtained for the Wenjiang station.

2.3. Definition of LLJ

Following the definitions of LLJ intensity (i.e., the peak wind speed at the jet nose) and the speed decay aloft [12,39,40], this study established a four-tier classification scheme for low-level jets. The detailed criteria are as follows. An LLJ-1 event requires a maximum wind speed of 10 m/s or higher within the lowest 3 km above ground level (AGL), coupled with a wind speed reduction of at least 5 m/s above the jet nose while remaining below 3 km. For LLJ-2 through LLJ-4, both thresholds are progressively elevated: the peak wind speed requirements become 12, 16, and 20 m/s, respectively, matched with decay standards of 6, 8, and 10 m/s. This system is hierarchical; for instance, the LLJ-1 category encompasses all stronger jets (i.e., LLJ-2 through LLJ-4). Furthermore, a persistence condition was imposed beyond the wind speed criteria: a jet was counted as valid only if its nose persisted for at least two consecutive hours, verified by examining the wind profiles one hour before and after each candidate event.

3. Results

In this section, the detection performance of the RWP is first evaluated. Based on this, the characteristics of the wind field and LLJs at this site are systematically investigated, with a focus on the vertical distribution, seasonal variation, and diurnal variation in horizontal wind, vertical wind, and LLJs of different intensities.

3.1. Radar Wind Profiler Performance Evaluation

The quality of RWP observations is influenced by multiple factors, including the inherent performance of the profiler, precipitation, spatial inhomogeneity of wind, and ground clutter. To better understand and utilize RWP wind field data, it is necessary to evaluate and analyze the performance of the RWP [41]. The three system performance indicators for radar performance evaluation include data acquisition rate (DAR), effective detection height, and data confidence [34]. The DAR is calculated as the ratio of data passing the confidence test to the total expected data at each altitude level [34]. Altitudes with a DAR above 0.8 are considered effective detection heights.

To quantitatively evaluate the wind measurement capability of the RWP, the monthly and diurnal variations in the DAR were statistically analyzed (Figure 2). The monthly mean DAR reached its maximum in October (98.7%) and its minimum in August (90.1%). From May to August, the DAR in the lower troposphere (2–4 km) was significantly lower than that in other months (Figure 2a). Differences in atmospheric temperature, humidity, and turbulence intensity are likely responsible for the monthly variations in DAR. The effective detection height of the RWP reached its minimum in January (7.4 km), while in some months it exceeded 8 km. Beyond the effective detection height, the DAR decreased rapidly with increasing altitude across all months. Regarding the diurnal variation characteristics of the DAR (Figure 2b), the DAR exhibited a unimodal distribution, peaking at 22:00 and reaching its minimum at 13:00. This diurnal pattern is likely associated with the daily cycle of atmospheric turbulence and convective activity. Strong turbulence in the afternoon (around 13:00) degrades data quality, while stable conditions at night (around 22:00) improve it, resulting in higher DAR at night and lower DAR in the afternoon.

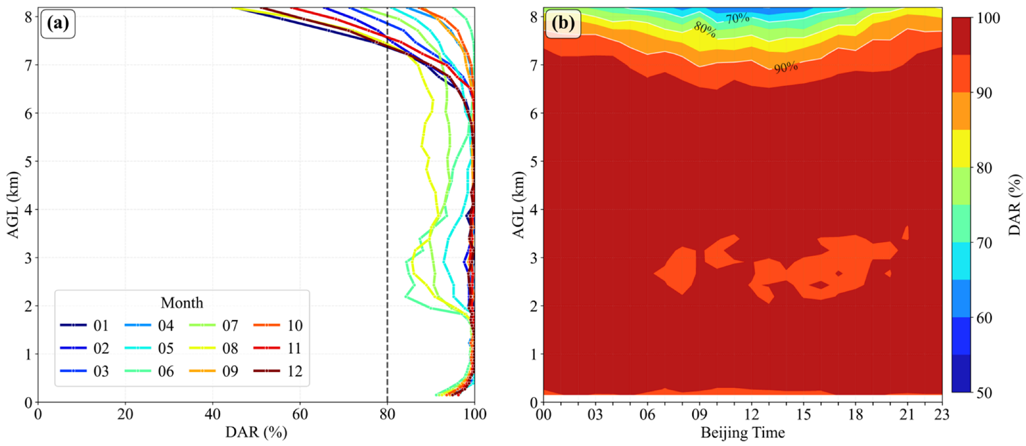

Figure 2. (**a**) Monthly data acquisition rate and (**b**) diurnal variation in data acquisition rate for the RWP.

To further evaluate the data quality of the RWP, a comparative verification was conducted between RWP data and synchronous balloon radiosonde observations. Balloon soundings are conducted twice daily (08:00 and 20:00). The RWP and radiosonde operate on different detection principles and observation times. To mitigate these discrepancies, RWP horizontal wind data closest to the radiosonde launch times were selected, and the nearest-neighbor interpolation method was applied to interpolate radiosonde winds to the corresponding RWP heights. The wind speed differences between the two systems were then calculated (Figure 3). Comparing the vertical distribution of mean errors in HWS, summer and autumn show small errors within ±1 m/s at all altitudes (Figure 3(a1–d1)). In spring and winter, errors remain within ±1 m/s below 4 km but increase to −1.79 m/s and −1.88 m/s at 4–6 km, respectively, indicating RWP underestimation at higher altitudes in cold seasons. Above 6 km, errors exceed −2 m/s in spring and exceed −3 m/s in winter at

6–8 km. One possible reason for the larger errors at higher altitudes in spring and winter is the enhanced upper-level westerly winds during these seasons. Stronger westerlies increase horizontal wind field inhomogeneity and also cause greater radiosonde balloon drift, both of which contribute to larger discrepancies between the fixed-point RWP and the drifting radiosonde. Zonal wind errors show similar patterns (Figure 3(a2–d2)), while meridional wind errors are generally smaller, with the best agreement in summer (Figure 3(a3–d3)), consistent with previous studies [49,50].

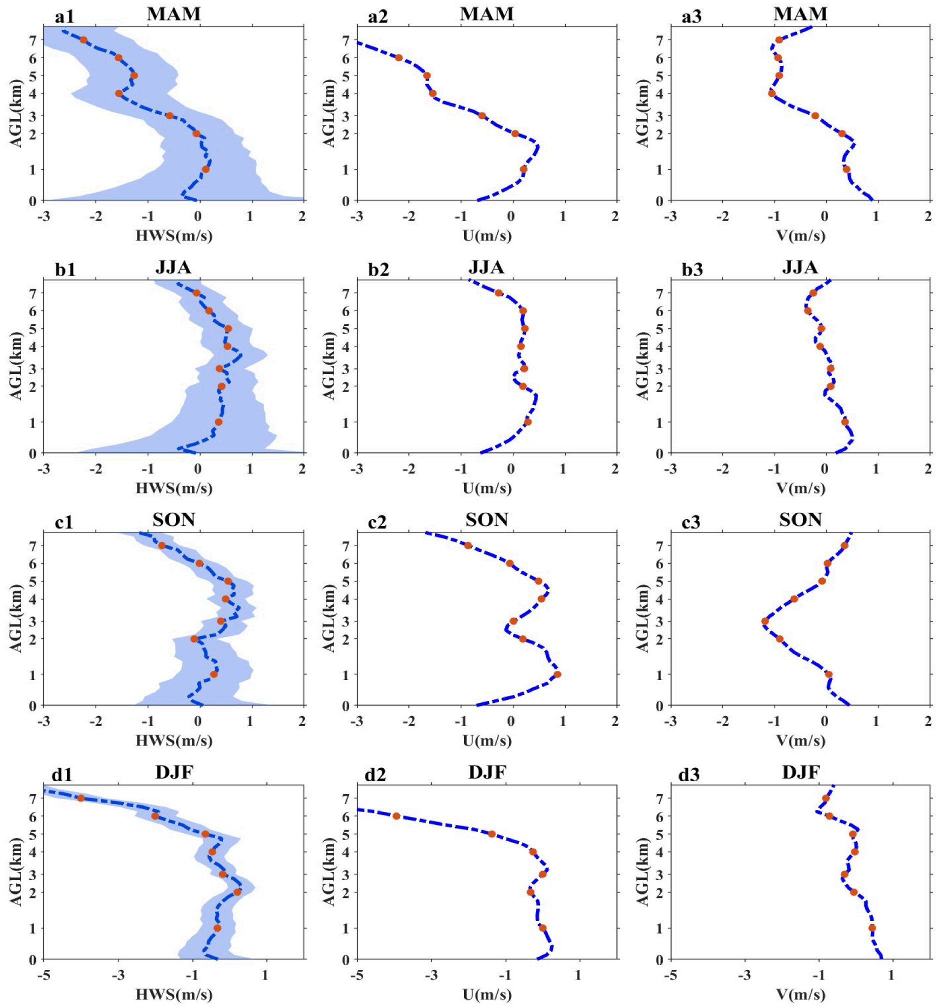

Figure 3. Vertical distribution of mean errors in HWS (**a1**–**d1**), zonal wind (**a2**–**d2**), and meridional wind (**a3**–**d3**) between radiosonde and RWP data across four seasons in Chengdu Wenjiang (blue curves represent mean errors, dark blue shading denotes root mean square errors, and red dots indicate mean errors at each kilometer altitude).

The statistical comparison between RWP and radiosonde HWS in the 0–6 km layer is summarized in Table 2. The mean bias ranges from −0.57 m/s in spring to 0.37 m/s in summer, with positive and negative values varying by season, indicating no systematic overestimation or underestimation. The root mean square error (RMSE) values range from 0.48 m/s in winter to 1.01 m/s in spring, and the correlation coefficients range from 0.57 in summer to 0.78 in winter. Notably, radiosonde observations are not an absolute reference. Balloon drift during ascent, particularly under strong winds, introduces spatial mismatches with fixed-point RWP measurements. This drift likely contributes to the larger discrepancies at higher altitudes, especially in spring and winter when the westerly jet is strongest. Nevertheless, the RWP and radiosonde data show good overall agreement in the 0–6 km layer.

Table 2. Statistical comparison between RWP and radiosonde HWS in the 0–6 km layer.

Season	Mean Bias (m/s)	RMSE (m/s)	Correlation Coefficient (r)
Spring (MAM)	−0.57	1.01	0.74
Summer (JJA)	0.37	0.76	0.57
Autumn (SON)	0.28	0.54	0.71
Winter (DJF)	−0.44	0.48	0.78

Note: Positive mean bias indicates RWP overestimates wind speed compared to radiosonde; negative indicates underestimation.

3.2. Vertical Distribution Characteristics of the Atmospheric Wind Field

Statistical analysis was conducted on the vertical distribution characteristics of HWS and HWD from RWP data (Figure 4). The prevailing wind direction is defined as the azimuth with the highest frequency of occurrence. The variations in mean wind profiles across seasons are shown in Figure 4a. The mean wind speed throughout the atmospheric column is highest in winter (8.0 m/s), followed by spring (7.3 m/s) and autumn (6.8 m/s), with the lowest mean wind speed occurring in summer (5.9 m/s). The mean wind speed increases with altitude in all seasons, with the greatest rate of increase observed in winter, rising from 2.0 m/s at the lowest level to 21.4 m/s at the highest level. In contrast, the wind speed increases most slowly in summer, rising from 3.3 m/s at the lowest level to 16.1 m/s at the highest level. Below 3 km, wind speeds are lowest in winter and highest in summer. Above 3 km, winter wind speeds gradually become the highest, while summer wind speeds become the lowest.

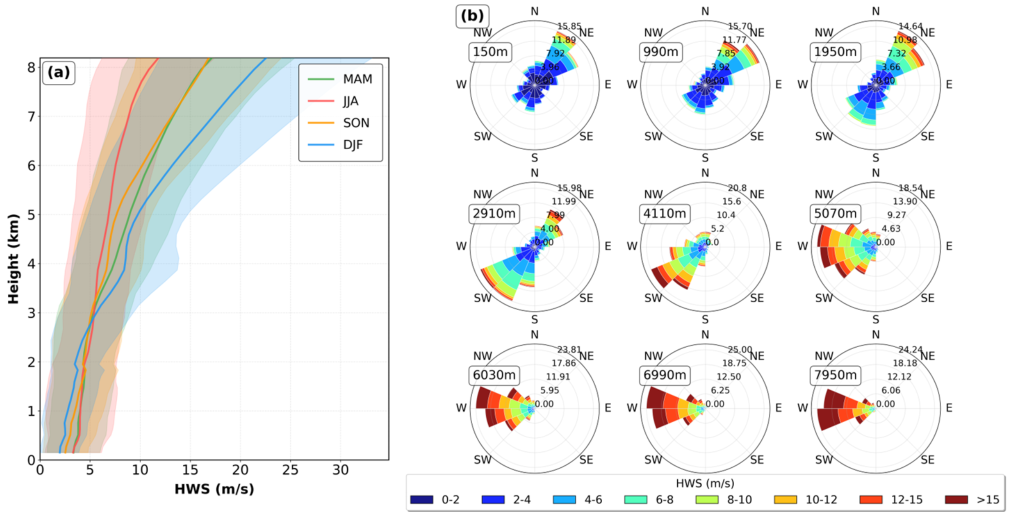

Figure 4. (**a**) Mean wind profiles across four seasons (shaded areas represent standard deviations), and (**b**) HWS and HWD rose diagrams at different altitudes.

Figure 4b presents the annual mean wind speed and direction rose diagrams for nine typical altitude levels (150 m, 990 m, 1950 m, 2910 m, 4110 m, 5070 m, 6030 m, 6990 m, and 7950 m). These levels were selected to uniformly cover the lower to upper troposphere (0–8 km). In the lower layer (below 2 km), the mean wind direction exhibits high variability, with the prevailing wind direction being northeasterly. Wind speeds are relatively low and increase slowly with height, with the mean wind speed rising from 2.7 m/s at 150 m to 4.1 m/s at 1950 m. In the middle layer (2–5 km), the prevailing wind direction shifts to southwesterly, and wind speeds increase with altitude, with the mean wind speed rising from 4.1 m/s at 1950 m to 8.4 m/s at 5070 m. In the upper layer (5–8 km), the prevailing wind direction is westerly, consistent with classical geostrophic wind theory. Wind speeds increase significantly with height, with the mean wind speed rising rapidly from 8.4 m/s at 5070 m to 15.8 m/s at 7950 m.

Further analysis was conducted on the probability distributions of HWD, HWS, and VWS with height (Figure 5). The vertical distribution characteristics of prevailing wind direction show slight variations across seasons (Figure 5(a1–a4)). In the lower layer (below 2 km), the prevailing wind directions are north–northeasterly and northeasterly. The dominant wind direction shifts from north-northeasterly in the lower boundary layer to northeasterly, which is largely consistent with the low-altitude wind field distribution observed at the Dayi station [48]. This phenomenon may be attributed to the blocking effects of the plateau and mountainous terrain, as well as the unique topography of the Sichuan Basin. Among the seasons, spring and winter exhibit a higher proportion of northeasterly winds, while summer and autumn have a higher proportion of north–northeasterly winds. In the middle layer (2–5 km), the prevailing wind directions are southerly and southwesterly, with the frequency distribution of wind directions tilting from southerly to southwesterly as altitude increases. In the upper layer (5–8 km), the prevailing wind direction is westerly, with the lowest proportion of prevailing westerly winds occurring in summer and the highest in winter. From summer to winter, the altitude of prevailing westerly winds decreases from 6 km to 5 km.

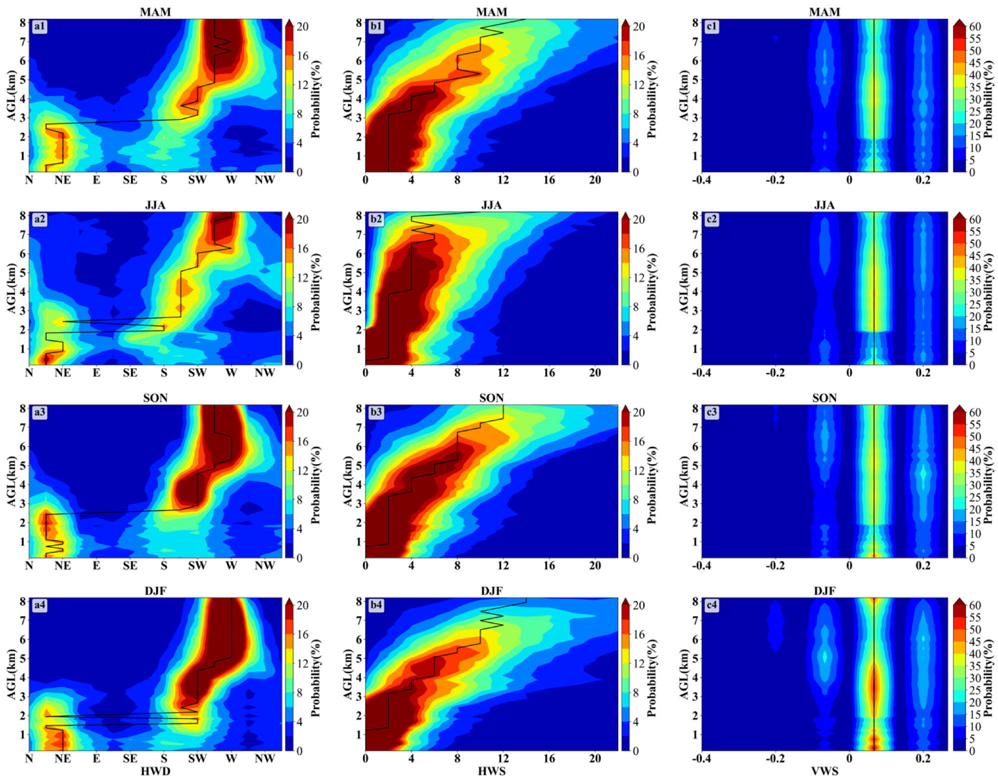

Figure 5. Probability distributions of horizontal wind direction (HWD, **a1**–**a4**), horizontal wind speed (HWS, **b1**–**b4**), and vertical wind speed (VWS, **c1**–**c4**) at different altitude levels across the four seasons. The subplots from the first to the fourth rows represent spring, summer, autumn, and winter, respectively, with solid lines indicating mean values.

In all four seasons, HWS increases slowly with height below 3 km and accelerates rapidly above 3 km (Figure 5(b1–b4)), similar to the frequency distribution of HWS in Hefei [25]. Moreover, the HWS in cold seasons is generally higher than in warm seasons, particularly in winter, when the HWS in the upper atmosphere can reach a maximum compared to other seasons. This may be attributed to the fact that the upper-level high-speed winds from the westerlies exhibit their maximum volume vertically from 500 hPa to 100 hPa during winter [51]. The HWS in the lower atmosphere is more concentrated than in the upper layers, consistent with the research findings of other scholars [23,25]. Regarding the vertical wind speed observed by the RWP, downward vertical velocity is defined as positive, and upward vertical velocity as negative [48]. The main distribution range of VWS is −0.2 to 0.2 m/s (Figure 5(c1–c4)), with the high-frequency center concentrated around 0.05 m/s, indicating the dominance of downdrafts. The prevailing subsidence at the Wenjiang site is likely related to the large-scale subsidence background over the western Sichuan Basin. Under stable weather conditions, the basin tends to experience weak downward motion, consistent with the observed positive mean vertical velocity. The high-frequency center is more concentrated in winter.

3.3. Diurnal Variation Characteristics of Atmospheric Wind Fields

The near-surface wind direction and speed in each season exhibit pronounced diurnal variations (Figure 6). The diurnal variation curves of near-surface wind speed show a unimodal pattern, with the peak wind speed occurring at 14:00 in all seasons, while the trough occurs before sunrise. Specifically, the trough appears at 07:00 in spring and autumn, at 06:00 in summer, and at 09:00 in winter. The peak near-surface wind speed is highest in spring, followed by summer, and lower in autumn and winter. Influenced by the mountain-valley breeze circulation, the prevailing near-surface wind direction is easterly (valley breeze) during the daytime afternoon (12:00–17:00) and northerly (mountain breeze) at night. In this study, nighttime refers to 20:00–07:00 local standard time (LST), defined based on the average sunrise (about 07:00 LST) and sunset (about 19:00 LST) times in Chengdu during the study period.

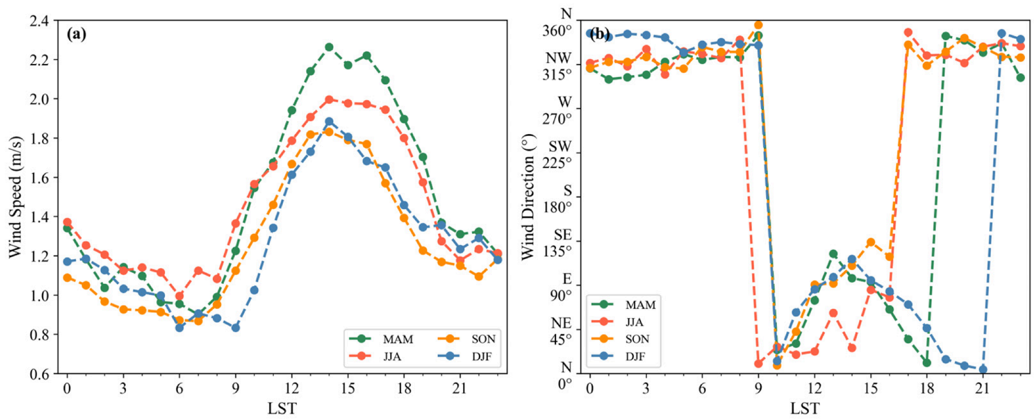

Figure 6. Diurnal variations in surface (**a**) wind speed and (**b**) wind direction across the four seasons.

The diurnal variation in vertical wind profiles within the planetary boundary layer is closely related to the dynamic and thermodynamic processes driven by the diurnal cycle of solar heating and longwave radiative cooling. Since westerly winds prevail above 6 km, the analysis focuses on the 0–6 km layer (Figure 7). The horizontal wind field exhibits pronounced seasonal and diurnal variations. Driven by mountain-valley breezes, the wind field below 1 km shows a clear diurnal cycle: easterly winds (valley breeze) dominate during the afternoon (12:00–17:00), shifting to northerly winds (mountain breeze) at night, with daytime wind speeds significantly lower than nighttime speeds. This circulation weakens with height. The wind field at altitudes of 1–2 km exhibits seasonal differences influenced by upper-level westerly winds. In spring and summer, easterly winds dominate throughout the day. In autumn, northeasterly winds dominate throughout the day, with westerly winds occurring during part of the daytime. In winter, westerly winds dominate near 1.5 km altitude during the daytime (08:00–16:00), shifting to northeasterly (19:00–21:00) and north-northeasterly (22:00–04:00) winds at night. With increasing altitude, the prevailing wind direction gradually transitions to westerly in all seasons. A notable feature in Figure 7 is the transition zone at 2–4 km altitude in summer, where the prevailing wind direction gradually shifts from easterly winds (controlled by mountain-valley breezes) to westerly winds (influenced by the westerly belt aloft). Overall, the influence of mountain-valley breezes weakens with height, while the westerly belt gradually becomes dominant, most notably in winter.

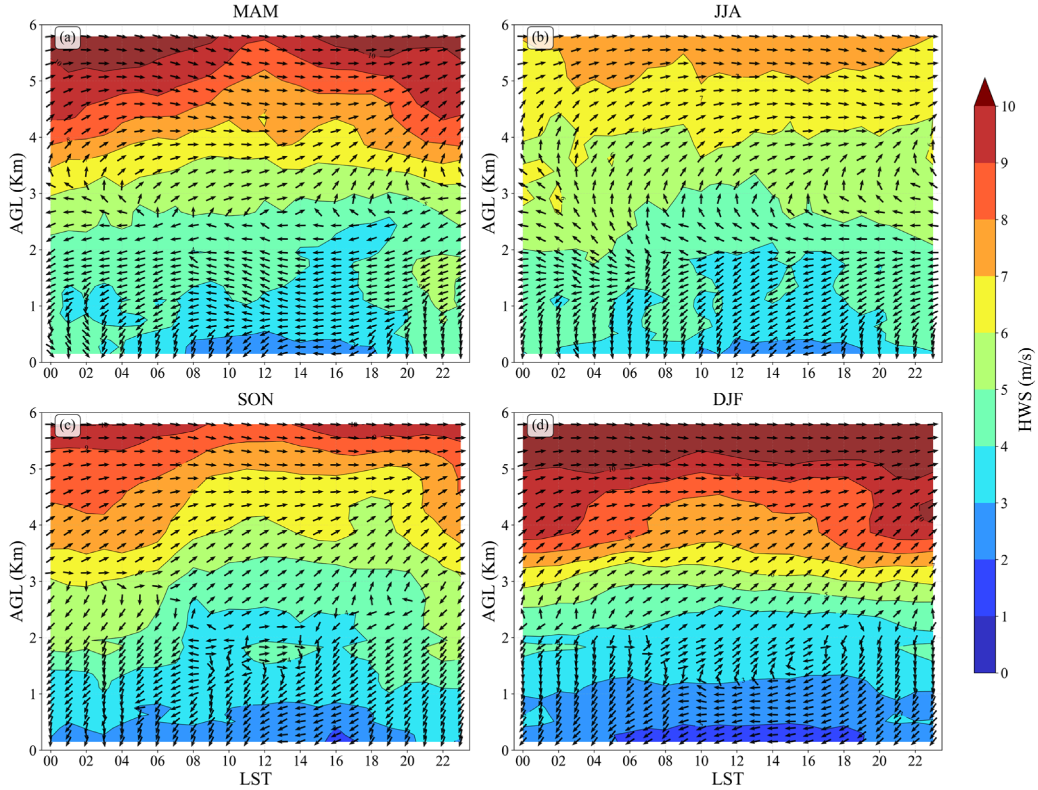

Figure 7. Diurnal variations in HWS and HWD in the middle and lower troposphere across seasons: (**a**) spring, (**b**) summer, (**c**) autumn, and (**d**) winter.

The upper-level wind field in each season exhibits a pronounced vertical gradient. Influenced by surface roughness, the near-surface HWS is the lowest, and wind speed increases significantly with height. In winter, due to stable atmospheric stratification, the average daily wind speed below 1 km is low (<3 m/s), which is unfavorable for the dispersion of surface pollutants and prone to the formation of heavy pollution episodes. The HWS at upper levels in each season exhibits typical diurnal variation characteristics, opposite to the pattern observed near the surface: the trough occurs during the daytime afternoon, while the peak occurs during nighttime hours. This phenomenon may be attributed to stronger turbulent activity during the day (especially in the afternoon), while the more stable atmospheric stratification and weaker turbulence at night lead to reduced wind energy dissipation, thereby resulting in higher nighttime wind speeds compared to daytime [25].

3.4. Analysis of LLJ Characteristics

Figure 8 shows the monthly variation in the occurrence frequency of four types of LLJs, where the monthly occurrence frequency is defined as the percentage of hours meeting the LLJ criteria in a given month. The peak frequency for all four LLJ types occurs in July (26.3%, 19.3%, 9.8%, and 2.7% for LLJ-1 to LLJ-4, respectively), followed by April (17.8%, 10.8%, 3.5%, and 1%, respectively). From a seasonal perspective, the occurrence frequency of the four LLJ types is highest in summer (14.2%, 9.4%, 4.1%, and 1.3% for LLJ-1 to LLJ-4, respectively), followed by spring (13.2%, 7.6%, 2.3%, and 0.7%) and autumn (10.8%, 5.4%, 1.4%, and 0.4%), and lowest in winter (5.8%, 2.6%, 0.7%, and 0).

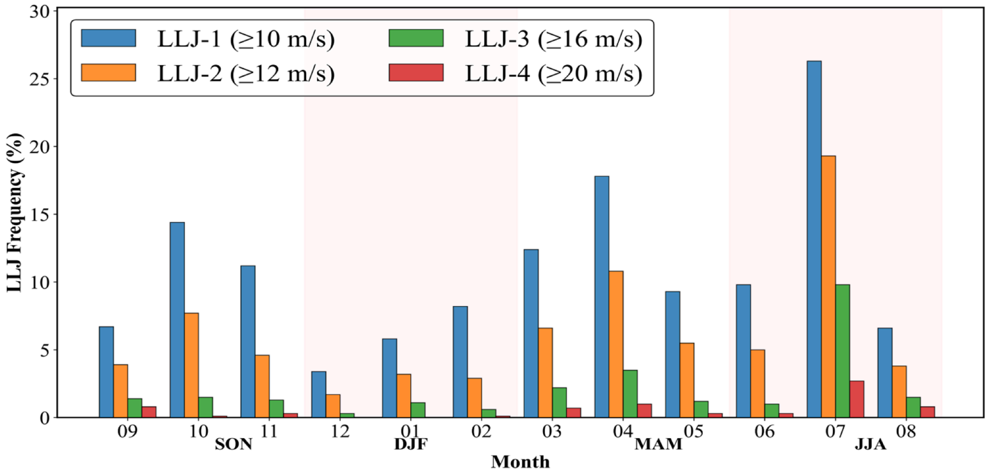

Figure 8. Monthly occurrence frequency of the four types of LLJs. The months falling in winter (DJF) and summer (JJA) are shaded in pink.

To further analyze the characteristics of LLJs, the occurrence frequencies of jet core wind speed, wind shear (defined as the wind speed difference between the surface and the jet height divided by the jet height), wind direction, and jet height were calculated (Figure 9). The average wind speed of LLJs in Chengdu is 15.1 m/s, with 78.2% below 18 m/s (Figure 9a). Strong LLJ-4 events account for 4.5%. The average wind shear is 0.02 s^{-1} (Figure 9b). The prevailing wind direction is north-northeasterly, followed by northeasterly (Figure 9c). Jet core heights are mainly distributed between 0.7 and 1.9 km, with the highest proportion for LLJ-3 and LLJ-4 at 1.3 km (Figure 9d).

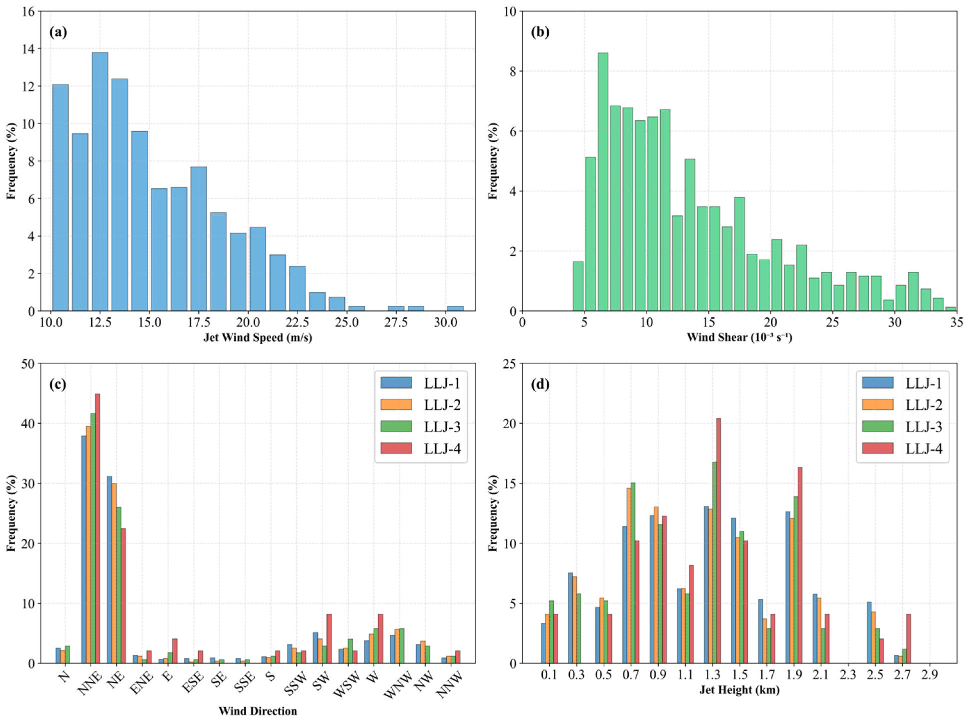

Figure 9. Frequency distribution of (**a**) wind speed, (**b**) wind shear, (**c**) wind direction, and (**d**) height of LLJs.

Figure 10 shows the wind field characteristics at the LLJs nose height across different seasons. In winter and spring, the dominant wind direction of LLJs is northeast, while in summer and autumn it is north-northeast, with the wind direction being more concentrated in summer and winter. The wind direction distribution of LLJs shows a clear correspondence with the background wind field presented in Figure 5 (i.e., the prevailing wind direction at the same altitude under non-LLJ conditions).

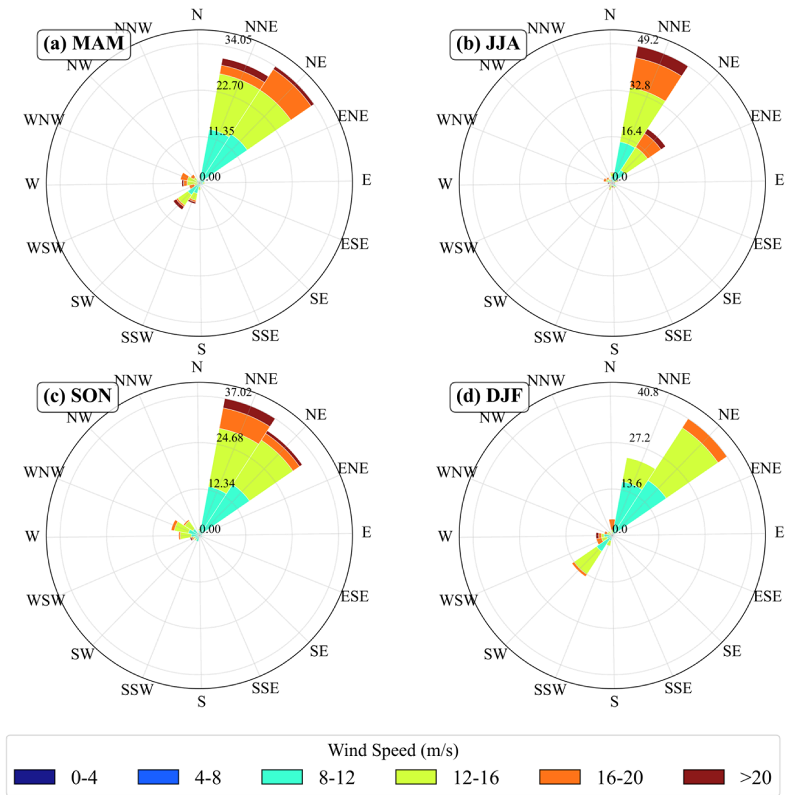

Figure 10. Wind rose diagrams of LLJs at nose height across seasons: (**a**) spring, (**b**) summer, (**c**) autumn, and (**d**) winter.

The diurnal variation in LLJs is influenced by surface heating/cooling cycles, atmospheric stability, and synoptic-scale weather patterns [25]. The total occurrence hours of LLJs (without persistence requirement) are summarized in Figure 11a. LLJ-1 occurred for 903 h (41.9% daytime, 58.1% nighttime), LLJ-2 for 514 h (42.0% daytime, 58.0% nighttime), LLJ-3 for 173 h (43.4% daytime, 56.6% nighttime), and LLJ-4 for 49 h (55.1% daytime, 44.9% nighttime). The peak hours are: LLJ-1 at 22:00 (57 h), LLJ-2 also at 22:00 (34 h), LLJ-3 at 18:00 (12 h), and LLJ-4 at 11:00 (4 h). Thus, LLJ-1 and LLJ-2 occur most frequently at night with a distinct peak at 22:00, while LLJ-3 peaks in the late afternoon (18:00) and LLJ-4 peaks around midday (11:00), suggesting that stronger jets may be more influenced by synoptic-scale forcing than by local diurnal circulation.

According to the classical inertial oscillation theory [22], nocturnal LLJs form due to the decoupling of nocturnal winds from surface friction, facilitated by the development of a near-surface temperature inversion. The nocturnal temperature inversion effectively reduces the influence of surface friction on the air above it [52]. Although daytime turbulent mixing reduces LLJ frequency, a considerable number of jets persist in the daytime boundary layer when the mixed layer develops weakly after sunrise and turbulence is insufficient to completely disrupt the nighttime jet structure [39].

A typical LLJ event (05:00 8 July 2024 to 18:00 10 July 2024, lasting 62 h) was selected to analyze the average wind speed profiles at different hours (Figure 11b). This event had the longest duration among all LLJ events identified in summer 2024, allowing a robust analysis of the diurnal evolution of jet intensity. Jet intensity increased after sunset, peaked at 02:00 (18.4 m/s), then decreased, with jet cores mostly below 1.4 km. Nighttime jet intensity was significantly higher than during the daytime.

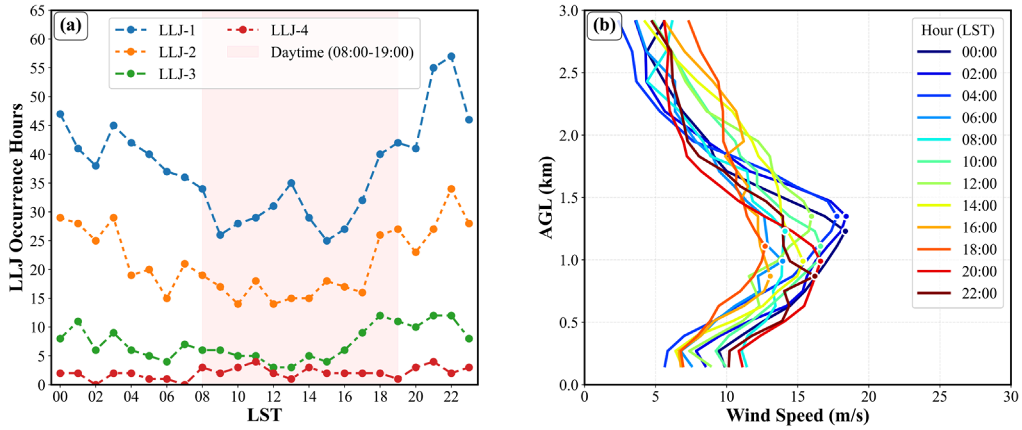

Figure 11. (**a**) Diurnal variation in occurrence hours for four types of LLJs (Pink shading indicates daytime), and (**b**) Average wind speed profiles at different hours for a typical LLJ event that occurred from 05:00 on 8 July 2024 to 18:00 on 10 July 2024 (the longest-duration LLJ in summer 2024).

4. Discussion

4.1. Comparison with Previous Studies

LLJ characteristics over Chengdu differ from those in other Chinese cities. Unlike the spring peak in Hefei [25] and winter-spring peak in Beijing [40], LLJs over Chengdu peak in summer (14.2% for LLJ-1), reflecting the combined effects of the East Asian monsoon, basin topography, and thermal contrast with the Tibetan Plateau. Jet core heights (0.7–1.9 km) are higher and more dispersed than in Shanghai (<0.6 km) [39] and Hefei (0.5–0.6 km) [25], likely due to a "basin effect" that deepens the boundary layer and enhances vertical mixing.

4.2. Physical Mechanisms

4.2.1. Nocturnal LLJ Peak and Inertial Oscillation

The higher frequency and intensity of LLJs at night are consistent with inertial oscillation theory [22]. Daytime turbulent mixing transfers momentum downward, reducing wind speeds aloft. After sunset, radiative cooling decouples the upper air from surface friction, allowing the wind to accelerate under pressure gradient and Coriolis forces, reaching a maximum at night.

4.2.2. Mountain-Valley Breeze Circulation

The diurnal variation below 1 km is controlled by mountain-valley breezes. The valley breeze (easterly) dominates in the afternoon as the basin warms faster than the mountains, while the mountain breeze (northerly) takes over at night as the slopes cool rapidly. This reversal is most pronounced in spring and summer, and least pronounced in winter when westerlies override local circulation. The vertical extent varies seasonally: in spring and summer, a deeper boundary layer allows the valley breeze to reach about 2 km; in autumn and winter, the shallower boundary layer confines it below 1 km, leaving higher levels exposed to westerly flow.

4.2.3. Seasonal Competition

This seasonal contrast leads to distinct wind regimes. In spring and summer, easterly winds persist up to 2 km throughout the day (Figure 7). In autumn and winter, westerly winds dominate above 1 km during the daytime. At 2–4 km in summer, a transition zone from easterlies to westerlies reflects competition between mountain-valley breezes and the westerly belt. In winter, strong westerlies dominate at lower altitudes, suppressing this transition zone.

4.3. Links to Large-Scale Circulation, Moisture Transport, and Precipitation

4.3.1. East Asian Monsoon Modulation

The seasonal variation in wind fields and LLJs is linked to the East Asian monsoon. Summer southwesterly monsoon enhances moisture transport into the basin, while winter westerly jet suppresses boundary layer development, explaining the wind shift at 2–5 km from southwesterly in summer to westerly in winter (Figure 5). Gao (2026) [53] classified summer synoptic patterns into three types based on the position of the western Pacific subtropical high. In Type 2 (31%), strong daytime radiative forcing enhances nocturnal southerly advection, transporting moisture from the South China Sea into the basin and promoting convection on the eastern slope of the Tibetan Plateau, providing a synoptic framework for our observed nocturnal LLJ peak.

4.3.2. LLJ-Driven Moisture Transport, Vortex Formation, and Basin Topography

The trumpet-shaped basin topography modulates LLJ-related moisture convergence. Wu (2022) [54] showed that clockwise rotation of the LLJ at 22:00 LST directs moisture toward the western basin, where convergence is enhanced by the trumpet-shaped topography. Zhang (2019) [55] found that net water vapor flux into the basin peaks at 22:00 LST, four hours before the precipitation peak at 02:00 LST, due to LLJ inertial oscillation. Beyond moisture transport, LLJs can directly force mesoscale vortex formation: Gao (2025) [56] found that the eastern Southwest Vortex is driven by LLJ terminal convergence, while the western vortex is thermally driven by downslope winds encountering warm-moist air.

A coherent sequence emerges: after sunset, inertial oscillation accelerates the LLJ [22]; by 22:00 LST, the LLJ peaks over Chengdu, coinciding with maximum moisture flux [54,55]; clockwise rotation directs moisture westward, enhanced by trumpet-shaped topography [54]; between 00:00 and 02:00 LST, LLJ convergence or downslope winds trigger vortex formation [56]; and precipitation peaks at 02:00 LST [55].

4.4. Limitations and Future Directions

This study has two limitations. First, it is based on a single site, which cannot capture the spatial variability of LLJs across the basin. Second, it is primarily statistical; case-specific LLJ events under different synoptic regimes were not investigated. Future work will expand to multiple sites and conduct process-based case studies under different synoptic patterns.

5. Conclusions

Based on one year of tropospheric wind profiler radar observations over Chengdu, this study systematically analyzed the vertical distribution, seasonal variation, and diurnal variation in the wind field and LLJs in the middle and lower troposphere. The main conclusions are as follows:

(1) The RWP maintains an effective detection height of at least 7.4 km throughout the year. Monthly data acquisition rates peak in October (98.7%) and reach a minimum in August (90.1%). Compared with radiosonde data, the RWP shows better consistency in summer and autumn, with absolute mean biases of 0.37 m/s and 0.28 m/s, respectively, versus 0.57 m/s in spring and 0.44 m/s in winter. Overall, horizontal wind speeds from the two systems agree well in the 0–6 km layer across all seasons.

(2) The annual mean wind speed is highest in winter (8.0 m/s), followed by spring (7.3 m/s) and autumn (6.8 m/s), and lowest in summer (5.9 m/s). Wind speed increases with height in all seasons, with the strongest vertical gradient in winter (from 2.0 m/s at the lowest level to 21.4 m/s at 8 km). Prevailing wind directions vary distinctly with altitude: north-northeasterly and northeasterly in the lower layer (0–2 km),

https://doi.org/10.3390/rs18111744

southerly and southwesterly in the middle layer (2–5 km), and westerly in the upper layer (5–8 km). Wind speed increases slowly below 3 km and rapidly above 3 km.

(3) Within the boundary layer (below 1 km), the wind field exhibits a clear diurnal cycle dominated by mountain-valley breezes: easterly winds (valley breeze) prevail during the afternoon (12:00–17:00), shifting to northerly winds (mountain breeze) at night. Surface wind speed peaks in the afternoon, while upper-level wind speed peaks at night. With increasing altitude, the influence of mountain-valley breezes weakens and the westerly belt becomes dominant, most notably in winter.

(4) LLJ occurrence frequency peaks in July (26.3% for LLJ-1), followed by April (17.8%). Seasonally, LLJ frequency is highest in summer (14.2% for LLJ-1), followed by spring (13.2%) and autumn (10.8%), and lowest in winter (5.8%). Most LLJ wind speeds are below 18 m/s (78.2%). The dominant LLJ direction is northeast in spring and winter, and north-northeast in summer and autumn. Jet core heights are mainly distributed between 0.7 and 1.9 km. For weaker LLJs (LLJ-1 and LLJ-2), both frequency and intensity are higher at night than during the day.

Author Contributions: Conceptualization, T.D.; methodology, T.D. and C.W.; software, T.D. and C.W.; validation, T.D.; formal analysis, T.D. and X.H.; investigation, T.D., X.H. and P.T.; resources, T.D.; data curation, T.D. and Y.S.; writing—original draft preparation, T.D.; writing—review and editing, P.T., Y.R. and J.D.; visualization, T.D. and C.W.; supervision, T.D.; project administration, T.D.; funding acquisition, T.D. All authors have read and agreed to the published version of the manuscript.

Funding: This research was supported by the National Key Research and Development Program of China (grant number 2023YFC3007501), the Heavy Rain and Drought-Flood Disasters in Plateau and Basin Key Laboratory of Sichuan Province (grant number SCQXKJQN202416), the National Natural Science Foundation of China (grant number 42405075), and the Natural Science Foundation of Chongqing (grant number CSTB2024NSCQ-MSX0612).

Data Availability Statement: The data used in this study are available upon request from the corresponding author due to privacy restrictions.

Acknowledgments: The authors thank Jian Wanlin from the Sichuan Meteorological Data Center for her support and assistance with the observational data. During the preparation of this manuscript, the authors used DeepSeek (https://chat.deepseek.com/) for the purposes of English language polishing and translation. The authors have reviewed and edited the output and take full responsibility for the content of this publication.

Conflicts of Interest: The authors declare no conflicts of interest.

Abbreviations

The following abbreviations are used in this manuscript:

LLJ	Low-Level Jet
RWP	Wind Profiler Radar
DAR	Data Acquisition Rate
AGL	Above the Ground Level
HWS	Horizontal Wind Speed
HWD	Horizontal Wind Direction
VWS	Vertical Wind Speed
MAM	March–April–May (spring)
JJA	June–July–August (summer)
SON	September–October–November (autumn)
DJF	December–January–February (winter)
RMSE	Root mean square error
LST	Local standard time

References

1. Liu, B.; Guo, J.; Gong, W.; Shi, Y.; Jin, S. Boundary Layer Height as Estimated from Radar Wind Profilers in Four Cities in China: Relative Contributions from Aerosols and Surface Features. *Remote Sens.* **2020**, *12*, 1657. [CrossRef]
2. Guo, J.; Liu, B.; Gong, W.; Shi, L.; Zhang, Y.; Ma, Y.; Zhang, J.; Chen, T.; Bai, K.; Stoffelen, A.; et al. Technical note: First comparison of wind observations from ESA's satellite mission Aeolus and ground-based radar wind profiler network of China. *Atmos. Chem. Phys.* **2021**, *21*, 2945–2958. [CrossRef]
3. Huang, J.; Ma, J.; Guan, X.; Li, Y.; He, Y. Progress in semi-arid climate change studies in China. *Adv. Atmos. Sci.* **2019**, *36*, 922–937. [CrossRef]
4. Huang, X.; Ding, A.; Gao, J.; Zheng, B.; Zhou, D.; Qi, X.; Tang, R.; Wang, J.; Ren, C.; Nie, W. Enhanced secondary pollution offset reduction of primary emissions during COVID-19 lockdown in China. *Natl. Sci. Rev.* **2021**, *8*, nwaa137. [CrossRef]
5. Stettner, D.; Velden, C.; Rabin, R.; Wanzong, S.; Daniels, J.; Bresky, W. Development of Enhanced Vortex-Scale Atmospheric Motion Vectors for Hurricane Applications. *Remote Sens.* **2019**, *11*, 1981. [CrossRef]
6. Yang, Y.; Fan, S.; Wang, L.; Gao, Z.; Zhang, Y.; Zou, H.; Miao, S.; Li, Y.; Huang, M.; Yim, S.H.L.; et al. Diurnal Evolution of the Wintertime Boundary Layer in Urban Beijing, China: Insights from Doppler Lidar and a 325-m Meteorological Tower. *Remote Sens.* **2020**, *12*, 3935. [CrossRef]
7. Wei, W.; Zhang, H.; Zhang, X.; Che, H. Low-level jets and their implications on air pollution: A review. *Front. Environ. Sci.* **2023**, *10*, 1082623. [CrossRef]
8. Smith, E.N.; Gebauer, J.G.; Klein, P.M.; Fedorovich, E.; Gibbs, J.A. The Great Plains Low-Level Jet during PECAN: Observed and Simulated Characteristics. *Mon. Weather Rev.* **2019**, *147*, 1845–1869. [CrossRef]
9. King, J.A.; Engelstaedter, S.; Washington, R.; Munday, C. Variability of the Turkana Low-Level Jet in Reanalysis and Models: Implications for Rainfall. *J. Geophys. Res. Atmos.* **2021**, *126*, e2020JD034154. [CrossRef]
10. Sánchez, M.P.; Pereira de Oliveira, A.; Varona, R.P.; Tito, J.V.; Codato, G.; Ynoue, R.Y.; Ribeiro, F.N.D.; Marques Filho, E.P.; da Silveira, L.C. Observational Investigation of the Low-Level Jets in the Metropolitan Region of São Paulo. *Earth Space Sci.* **2022**, *9*, e2021EA002190. [CrossRef]
11. Ma, X.; Li, Y.; Li, Z.; Huo, F. Investigation of the characteristics of low-level jets over North America in a convection-permitting Weather Research and Forecasting simulation. *Atmos. Chem. Phys.* **2024**, *24*, 12013–12030. [CrossRef]
12. Bonner, W.D. CLIMATOLOGY OF THE LOW LEVEL JET. *Mon. Weather Rev.* **1968**, *96*, 833–850. [CrossRef]
13. Ding, J.; Ren, Y.; Zhang, H.; Chang, H.; Hu, Z.; Liang, J.; Zhang, K.; Wang, S.; Cao, X.; Tian, P.; et al. Mechanism of Turbulence Structure Evolution in the Nocturnal Boundary Layer During the Interaction of Low-Level Jet and Internal Gravity Waves: Based on Full Boundary Layer Turbulence Observations. *J. Geophys. Res. Atmos.* **2025**, *130*, e2024JD042106. [CrossRef]
14. Du, Y.; Chen, G. Climatology of Low-Level Jets and Their Impact on Rainfall over Southern China during the Early-Summer Rainy Season. *J. Clim.* **2019**, *32*, 8813–8833. [CrossRef]
15. Wei, W.; Zhang, H.; Wu, B.; Huang, Y.; Cai, X.; Song, Y.; Li, J. Intermittent turbulence contributes to vertical dispersion of PM 2.5 in the North China Plain: Cases from Tianjin. *Atmos. Chem. Phys.* **2018**, *18*, 12953–12967. [CrossRef]
16. Hu, X.-M.; Klein, P.M.; Xue, M.; Zhang, F.; Doughty, D.C.; Forkel, R.; Joseph, E.; Fuentes, J.D. Impact of the vertical mixing induced by low-level jets on boundary layer ozone concentration. *Atmos. Environ.* **2013**, *70*, 123–130. [CrossRef]
17. Céspedes, J.; Kotthaus, S.; Preissler, J.; Toupoint, C.; Thobois, L.; Drouin, M.A.; Dupont, J.C.; Faucheux, A.; Haeffelin, M. The Paris low-level jet during PANAME 2022 and its impact on the summertime urban heat island. *Atmos. Chem. Phys.* **2024**, *24*, 11477–11496. [CrossRef]
18. Zhang, X.; Luo, Y.; Du, Y. Observation of Boundary-Layer Jets in the Northern South China Sea by a Research Vessel. *Remote Sens.* **2024**, *16*, 3872. [CrossRef]
19. Han, Z.; Ge, J.; Chen, X.; Hu, X.; Yang, X.; Du, J. Dust activities induced by nocturnal low-level jet over the Taklimakan desert from WRF-Chem simulation. *J. Geophys. Res. Atmos.* **2022**, *127*, e2021JD036114. [CrossRef]
20. Lin, Y.; Wang, C.; Yan, J.; Li, J.; He, S. Observation and Simulation of Low-Level Jet Impacts on 3D Urban Heat Islands in Beijing: A Case Study. *J. Atmos. Sci.* **2022**, *79*, 2059–2073. [CrossRef]
21. Chen, Y.; Tu, C.; Hsiao, F.; Chen, C.; Lin, P.; Lin, P. An overview of low-level jets (LLJs) and their roles in heavy rainfall over the Taiwan area during the early summer rainy season. *Meteorology* **2022**, *1*, 64–112. [CrossRef]
22. Blackadar, A.K. Boundary layer wind maxima and their significance for the growth of nocturnal inversions. *Bull. Am. Meteorol. Soc.* **1957**, *38*, 283–290. [CrossRef]
23. Zheng, J.; Liu, Y.; Peng, T.; Wan, X.; Huang, X.; Wang, Y.; Che, Y.; Xu, D. Investigating Wind Characteristics and Temporal Variations in the Lower Troposphere over the Northeastern Qinghai–Tibet Plateau Using a Doppler LiDAR. *Remote Sens.* **2024**, *16*, 1840. [CrossRef]
24. Zong, L.; Yang, Y.; Xia, H.; Yuan, J.; Guo, M. Elucidating the impacts of various atmospheric ventilation conditions on local and transboundary ozone pollution patterns: A case study of Beijing, China. *J. Geophys. Res. Atmos.* **2023**, *128*, e2023JD039141. [CrossRef]

25. Wei, T.; Wang, M.; Wu, K.; Yuan, J.; Xia, H.; Lolli, S. Characterizing urban planetary boundary layer dynamics using 3-year Doppler wind lidar measurements in a western Yangtze River Delta city, China. *Atmos. Meas. Tech.* **2025**, *18*, 1841–1857. [CrossRef]
26. Zhou, X.; Zhang, C.; Li, Y.; Chen, Z.; Zhang, J.; Ding, X. Wind gust parameters in the lower troposphere based on Doppler Lidar data. *J. Geophys. Res. Atmos.* **2023**, *128*, e2022JD038156. [CrossRef]
27. Rubio, H.; Kühn, M.; Gottschall, J. Evaluation of low-level jets in the southern Baltic Sea: A comparison between ship-based lidar observational data and numerical models. *Wind Energy Sci. Discuss.* **2022**, *7*, 2433–2455. [CrossRef]
28. Li, X.; Du, Y. Statistical relationships between two types of heavy rainfall and low-level jets in South China. *J. Clim.* **2021**, *34*, 8549–8566. [CrossRef]
29. Sun, X.; Zhou, Y.; Zhao, T.; Bai, Y.; Huo, T.; Leng, L.; He, H.; Sun, J. Effect of vertical wind shear on $PM_{2.5}$ changes over a receptor region in Central China. *Remote Sens.* **2022**, *14*, 3333. [CrossRef]
30. Yan, Y.; Cai, X.; Wang, X.; Miao, Y.; Song, Y. Low-Level Jet Climatology of China Derived From Long-Term Radiosonde Observations. *J. Geophys. Res. Atmos.* **2021**, *126*, e2021JD035323. [CrossRef]
31. Dolman, B.K.; Reid, I.M.; Tingwell, C. Stratospheric tropospheric wind profiling radars in the Australian network. *Earth Planets Space* **2018**, *70*, 170. [CrossRef]
32. Liu, B.; Ma, Y.; Guo, J.; Gong, W.; Zhang, Y.; Mao, F.; Li, J.; Guo, X.; Shi, Y. Boundary layer heights as derived from ground-based radar wind profiler in Beijing. *IEEE Trans. Geosci. Remote Sens.* **2019**, *57*, 8095–8104. [CrossRef]
33. Ishihara, M.; Kato, Y.; Abo, T.; Kobayashi, K.; Izumikawa, Y. Characteristics and performance of the operational wind profiler network of the Japan Meteorological Agency. *J. Meteorol. Soc. Jpn. Ser. II* **2006**, *84*, 1085–1096. [CrossRef]
34. Liu, B.; Guo, J.; Gong, W.; Shi, L.; Zhang, Y.; Ma, Y. Characteristics and performance of wind profiles as observed by the radar wind profiler network of China. *Atmos. Meas. Tech.* **2020**, *13*, 4589–4600. [CrossRef]
35. Wei, W.; Wu, B.G.; Ye, X.X.; Wang, H.X.; Zhang, H.S. Characteristics and Mechanisms of Low-Level Jets in the Yangtze River Delta of China. *Bound.-Layer Meteorol.* **2013**, *149*, 403–424. [CrossRef]
36. Deng, X.; He, D.; Zhang, G.; Zhu, S.; Dai, R.; Jin, X.; Fu, W.; Shen, W.; Chen, J.; Fan, Y. Comparison of horizontal wind observed by wind profiler radars with ERA5 reanalysis data in Anhui, China. *Theor. Appl. Climatol.* **2022**, *150*, 1745–1760. [CrossRef]
37. Solanki, R.; Guo, J.; Lv, Y.; Zhang, J.; Wu, J.; Tong, B.; Li, J. Elucidating the atmospheric boundary layer turbulence by combining UHF radar wind profiler and radiosonde measurements over urban area of Beijing. *Urban Clim.* **2022**, *43*, 101151. [CrossRef]
38. Li, N.; Guo, J.; Wu, M.; Zhang, F.; Guo, X.; Sun, Y.; Zhang, Z.; Liang, H.; Chen, T. Low-level jet and its effect on the onset of summertime nocturnal rainfall in Beijing. *Geophys. Res. Lett.* **2024**, *51*, e2024GL110840. [CrossRef]
39. Wei, W.; Zhang, H.; Ye, X. Comparison of low-level jets along the north coast of China in summer. *J. Geophys. Res. Atmos.* **2014**, *119*, 9692–9706. [CrossRef]
40. Miao, Y.; Guo, J.; Liu, S.; Wei, W.; Zhang, G.; Lin, Y.; Zhai, P. The Climatology of Low-Level Jet in Beijing and Guangzhou, China. *J. Geophys. Res. Atmos.* **2018**, *123*, 2816–2830. [CrossRef]
41. Yang, K.; Gao, Z.; Gao, B.; Xiao, T.; Yang, G. Spatiotemporal Distribution Characteristics Research of Wind Field and Wind Shear on the East Coast of Erhai Lake in the Southeast Edge of Hengduan Mountain Area. *Plateau Meteorol.* **2025**, *44*, 462–474.
42. Li, N.; Guo, J.; Guo, X.; Chen, T.; Zhang, Z.; Tang, N.; Wang, Y.; Yang, H.; Zheng, Y.; Zhou, Y. On the nationwide variability of low-level jets prior to warm-season nocturnal rainfall in China revealed by radar wind profilers. *Atmos. Chem. Phys.* **2026**, *26*, 3339–3356. [CrossRef]
43. Wang, J.; Zhang, Q.; Zhang, T.; Long, K.; Shi, R. Low-level Wind Field Characteristic Observed by Wind Profile Radar During Two Rainstorm Processes in Chengdu. *J. Arid Meteorol.* **2021**, *39*, 87–95.
44. Zhang, H.; Zhou, Y.; Lai, Z.; Deng, G. Overshooting convection and torrential precipitation associated with the mesoscale northerly low-level jets in the Sichuan Basin, China. *Atmos. Res.* **2024**, *310*, 107604. [CrossRef]
45. Hu, D.; Xie, X.; Chen, C.; Zhou, Q. Wind Field Characteristics of Heavy Precipitation Process in Western Sichuan Basin Based on Wind Profiler Radar Data. *Plateau Meteorol.* **2025**, *44*, 240–252.
46. Xiong, J.; Li, J.; Gao, F.; Zhang, Y. City wind impact on air pollution control for urban planning with different time-scale considerations: A case study in Chengdu, China. *Atmosphere* **2023**, *14*, 1068. [CrossRef]
47. Lei, Y.; Wu, K.; Zhang, X.; Kang, P.; Du, Y.; Yang, F.; Fan, J.; Hou, J. Role of meteorology-driven regional transport on O3 pollution over the Chengdu Plain, southwestern China. *Atmos. Res.* **2023**, *285*, 106619. [CrossRef]
48. Cao, Y.; Zhao, X.; Su, D.; Cheng, X. Analysis of Horizontal Wind Field Regional Difference within Boundary Layer in Chengdu West Mountainous Area and Plain Transition Area Based on Wind Profile Radar. *Meteorol. Sci. Technol.* **2024**, *52*, 743–752.
49. Zhu, L. Preliminary Quality Analysis of Horizontal Wind Products from Wind Profiler Radar for Data Assimilation. *Meteorol. Mon.* **2015**, *41*, 1494–1502.
50. Wang, Y.; Zhang, W.; Zhao, Y. Analysis of Wind Characteristics of Wind-Profiler Radars and Their Quality Control Methods for Data Assimilation. *Chin. J. Atmos. Sci.* **2021**, *45*, 123−147.
51. Yao, H.; Li, D. Spatial Structure of East Asia Subtropical Jet Stream and Its Relation with Winter Air Temperature in China. *Chin. J. Atmos. Sci.* **2024**, *37*, 881–890.

52. Mirza, A.K.; Dacre, H.F.; Lo, C.H.B. A case study analysis of the impact of a new free tropospheric turbulence scheme on the dispersion of an atmospheric tracer. *Q. J. R. Meteorol. Soc.* **2024**, *150*, 1907–1925. [CrossRef]
53. Gao, Z.; Li, L.; Zhao, C.; Gao, G.; Jiang, R.; Yang, H.; Liu, S.; Lu, P. Impacts of Distinct Synoptic Patterns on Fine-Scale Precipitation Characteristics in Complex Terrain of Southwestern China. *Int. J. Climatol.* **2026**, e70315. [CrossRef]
54. Wu, A.; Li, G. Roles of the topographically-affected boundary layer low-level jet in the moisture transport process of nocturnal rainstorms in mountainous areas around the western Sichuan basin. *Atmosphere* **2022**, *14*, 84. [CrossRef]
55. Zhang, Y.; Xue, M.; Zhu, K.; Zhou, B. What is the main cause of diurnal variation and nocturnal peak of summer precipitation in sichuan basin, China? the key role of boundary layer low-level jet inertial oscillations. *J. Geophys. Res. Atmos.* **2019**, *124*, 2643–2664. [CrossRef]
56. Gao, G.; Jiang, X.; Gao, Z.; Feng, Y.; Dong, Y.; Xiao, D.; Zhang, P.; Li, J.; Yang, Y. The early formation processes of the dual southwest vortices: Different horizontal scales and generation mechanisms. *Q. J. R. Meteorol. Soc.* **2025**, *151*, e5056. [CrossRef]